



Publication Year	2018
Acceptance in OA	2020-11-19T12:20:26Z
Title	Systematic study of the cross polarization introduced by broadband antireflection layers at microwave frequencies
Authors	Tapia, Valeria, Rodríguez, Rafael, Reyes, Nicolás, Patricio Mena, F., Yagoubov, Pavel, CUTTAIA, FRANCESCO, Bronfman, Leonardo
Publisher's version (DOI)	10.1364/AO.57.009223
Handle	http://hdl.handle.net/20.500.12386/28448
Journal	APPLIED OPTICS
Volume	57



Systematic study of the cross polarization introduced by broadband antireflection layers at microwave frequencies

VALERIA TAPIA,^{1,2}  RAFAEL RODRÍGUEZ,^{1,3,4} NICOLÁS REYES,^{5,*}  F. PATRICIO MENA,⁵ PAVEL YAGOUBOV,⁶ FRANCESCO CUTTAIA,⁷ AND LEONARDO BRONFMAN¹

¹Astronomy Department, Universidad de Chile, Camino El Observatorio 1515, Las Condes, Chile

²Electrical Engineering Department, Eindhoven University of Technology, De Zaale, 5600MB, Eindhoven, The Netherlands

³CePIA, Astronomy Department, Universidad de Concepción, Casilla 160-C, Concepción, Chile

⁴Institute of Electricity and Electronics, Universidad Austral, General Lagos 2086, Valdivia, Chile

⁵Electrical Engineering Department, Universidad de Chile, Av. Tupper 2007, Santiago Centro, Chile

⁶European Southern Observatory, Karl-Schwarzschild-Str. 2, 85748 Garching bei München, Germany

⁷Osservatorio di Astrofisica e Scienza dello Spazio di Bologna, Via Gobetti 101, 40129, Bologna, Italy

*Corresponding author: nireyes@uchile.cl

Received 10 August 2018; revised 28 September 2018; accepted 1 October 2018; posted 2 October 2018 (Doc. ID 341988); published 25 October 2018

Implementation of antireflection layers using structured materials is of common use in millimeter- and sub-millimeter-wave refractive optic systems. In this work we have systematically studied the effect of such structures in the optical propagation with special emphasis on the cross polarization they introduce. We have performed extensive simulations and experimental verification of several commonly used structures: concentric grooves, parallel grooves, an array of boxes, an array of cylinders, and rectangular- versus triangular-shaped grooves. As a result, we propose optimal structures for demanding applications in terms of polarization and return losses over large fractional bandwidths. © 2018 Optical Society of America

<https://doi.org/10.1364/AO.57.009223>

1. INTRODUCTION

When part of an optical system, refractive components, such as lenses, filters, or windows, suffer from material losses that need to be minimized before achieving the best performance. In particular, reflected waves produce an effective power loss and also generate several undesired effects such as interference, standing waves, and coupling to unwanted directions that degrade the radiation performance. As a consequence, the pattern could present an increment of the sidelobe level, deformation of the main beam shape, undesired phase front modifications, and an increment in the cross-polar content.

Reflection losses are produced when an electromagnetic wave travels from one medium to another. To reduce power loss, a classical and effective strategy is to include one or more adaptation layers. For an interface between two dielectric materials of refractive indexes n_d and n_0 , the ideal single antireflective layer has a refractive index of $n_m = \sqrt{n_d \cdot n_0}$ and a thickness of $\lambda/(4n_m)$ [1].

The actual implementation of the adaptation layers depends on the frequency of operation. At high frequencies, beyond the infrared, where the matching layer has a thickness of a few tens of microns, the implementation is rather straightforward.

The required material is coated onto the surface of the optical component. However, at microwave and millimeter frequencies, the required layers are much thicker, requiring other implementations. A commonly used strategy is to imprint an artificial material, in the form of periodic structures, over the surface of the dielectric material. This implementation has two main advantages. First, it is easier to implement, especially over curved or discontinuous shapes. Second, artificial materials can be fabricated with any desired effective refractive index.

The geometry of the periodic structure controls the index of refraction of the artificial material. It is important to consider that the size of the unit cell has to be much smaller than the operation wavelength to appropriately mimic the desired refractive index. Although different structures can be used, the most common geometries are triangular and rectangular grooves, mainly because of the manufacturing simplicity [2–7]. Other common structures are boxes and cylinders implemented as either pillars or cavities [8–10].

It is a well-established fact that by choosing the appropriate geometrical parameters, a good matching layer can be achieved, resulting in low reflection losses. Nevertheless, the shape of the structure creates other undesired effects, as astigmatism in

lenses and variation of the direction of the polarization, affecting the cross polarization of the optical system [11,12]. Another important effect is the intrinsically limited bandwidth achieved by these structures, caused by the specific thickness of the antireflection layer.

The polarization of a general wave propagating from one medium to another can be described as a linear combination of parallel and perpendicular polarizations with respect to the direction of propagation. Considering transmission-line theory, the dielectric constant of a quarter-wavelength matching layer can also be decomposed in parallel and perpendicular components [13]. Achieving perfect matching for both polarizations is only possible for normal incidence, where $n_{\theta_i=0} = n_{m\parallel} = n_{m\perp}$. However, in practice, the working range can be extended to small angles. For incident angles larger than 30 deg, the differences between the polarizations become significant, having differences larger than 10%. Correspondingly, when periodic structures are used as antireflective layers, the angle of incidence also produces modification on the dielectric constant due to the interaction of the wave with the geometry.

In Ref. [11] an analysis of the phase difference produced by the circular grooves' layer on dielectric components is presented. Following this cross-polarization analysis, let us consider an incident wave with the electric field oriented in the y -axis, $\vec{E}_i = \vec{E}_i \cdot \vec{a}_y$. Let us also consider an antireflective layer with a geometrical structure oriented in an angle Ψ relative to the polarization plane. If the layer introduces a phase delay δ , the transmitted field can be written as

$$\begin{aligned} \vec{E}_t = & E_i \cos(\Psi) \sin(\Psi) (1 - e^{j\delta}) \vec{a}_x \\ & + E_i (\sin(\Psi)^2 + \cos(\Psi)^2) e^{j\delta} \vec{a}_y. \end{aligned} \quad (1)$$

It can be noticed that if the geometrical structures of the antireflective layer are parallel or normal to the electric field of the wave, the first term disappears introducing no cross polarization. In any other case, the linear polarizations are transformed into elliptical components, generating some amount of cross polarization. Apart from this, it should be pointed out that even surfaces without antireflective layers can generate cross polarization depending on the shape of the dielectric.

Scientific literature extensively analyzes antireflective structures from the point of view of reflection losses [6,14,15]. Although less discussed in literature, the introduction of cross polarization is also critical in several high-performance applications [6,16]. For example, antireflective layers are

especially important for sensitive systems, such as radio telescopes, since they have to be included in dielectric lenses, infrared filters, and vacuum windows. Low reflection losses contribute to better receiver noise temperature, while low cross polarization allows higher polarization efficiencies to be obtained, resulting in better polarization sensitivity of the instrument.

To compare the performance of different geometrical structures commonly used as antireflective layers in radio astronomy, we have studied five different profiles. We start by presenting their design and optimization based on simulation. Later, we show the characterization of three of the profiles: concentric rectangular grooves, perpendicular triangular grooves, and a two-cylinder layer. All the antireflective structures were designed to work in the frequency range between 67 and 116 GHz. This range represents a fractional bandwidth of 53%, the largest in any astronomical receiver, so far. The motivation to use this frequency range is to apply the best antireflective structure to the optics of the new Band-2 + 3 receivers for the Atacama Large Millimeter/submillimeter Array (ALMA) [17,18].

2. DESIGN AND SIMULATION

We have chosen high-density polyethylene (HDPE) as the test material. HDPE is a plastic material that has an extended use in high-tech optical applications. It is a low-loss material at microwave and millimeter frequencies, $\tan \delta \approx 2.3 \cdot 10^{-4}$, having a moderately high refractive index, $n \approx 1.53$ [19].

We have selected five different geometric structures as test antireflective layers (Fig. 1). We have carefully chosen the geometries to exemplify the most common structures used as antireflective layers [8,20–22]. To compare different spatial distributions, we have implemented two concentric circular structures (using rectangular and triangular grooves), two perpendicular geometries (using boxes and triangular grooves), and one cylinder-based geometry on a honeycomb distribution. The selected structures also serve to compare the use of multiple layers to different effective refraction indexes. We consider three cases: a single layer of rectangular grooves, two examples of two-layer systems (using boxes and cylinders), and an *infinite-layer* system formed by triangular grooves where the effective refraction index varies continuously with depth. Moreover, all the studied structures can be straightforwardly implemented using modern computer numerical control

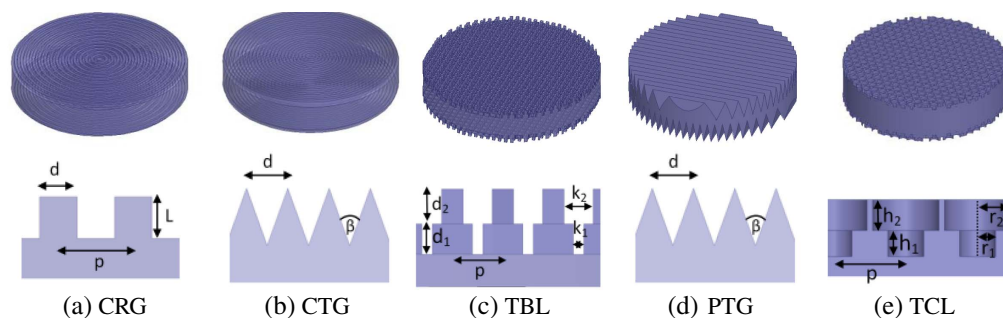


Fig. 1. Simulated antireflective layers. (a) Concentric rectangular grooves (CRG). (b) Concentric triangular grooves (CTG). (c) Two-box layer (TBL). (d) Perpendicular triangular grooves (PTG). (e) Two-cylinder layer (TCL).

(CNC) machining tools. For example, the concentric structures can be easily implemented using a lathe. The perpendicular geometries could be manufactured using milling cutter machining, and the cylindrical distribution could be implemented using a drill.

Having chosen the geometrical structures, the next step was to optimize their geometrical parameters to minimize reflection losses and cross polarization. This task was done using the High Frequency Structure Simulator software from Ansys. We used genetic-algorithm optimization to ensure a global minimum is found. Mechanical restrictions were used as optimization restrictions of the problem. To simulate the structure response to a plane wave we used equivalent models based on the master-slave condition and Floquet ports, even when some layers did not have planar-periodic structures. Floquet-port simulations propagate plane waves faster than full models, and the optimization parameters can be directly calculated without postprocessing. Afterward, special considerations were made for nonplanar periodic layers, such as concentric grooves. We have created simplified models considering only a part of the structure but sufficiently large for a good characterization. We have also checked that the simulation results did not change considerably when a portion of the model was added or subtracted.

The values obtained after the first optimization were used as starting point for the next fine-tuning simulations. These posterior simulations correspond to an open model, excited using a planar-wave stimulus. This excitation impinges over a cylindrical slab that supports the antireflection layer. The slab thickness was chosen to be 2 times the central wavelength. The geometric parameters that were optimized are shown in Fig. 1. The goals of the optimization were minimizing reflection losses and the cross-polarization level on the output beam. Final geometrical parameters are consistent with similar optimized antireflection layers in the literature taking into consideration the wavelength scale [7,13,20].

To compare the cross-polarization performance of the samples, we have selected as the figure of merit the polarization efficiency. Polarization efficiency is defined as the ratio between

Table 1. Best Parameters for Minimizing Reflection Losses in the Five Analyzed Antireflection Structures^a

CRG	CTG	TBL	PTG	TCL
$d = 0.54$	$d = 0.80$	$d_1 = 0.64$	$d = 0.64$	$r_1 = 0.73$
$p = 1.00$	$\beta = 20.00^\circ$	$d_2 = 0.73$	$\beta = 20.00^\circ$	$r_2 = 0.40$
$L = 0.50$		$k_1 = 0.22$		$b_1 = 0.68$
		$k_2 = 0.61$		$b_2 = 0.57$
		$p = 1.06$		$p = 1.59$

^aParameters are in millimeters unless specified otherwise.

the power in the output copolar fields and the total power in the output complete fields (copolar plus cross polar). When a Gaussian beam propagates through the structure, this power is calculated as the integral of the squared fields over a specific angle. In this study we have chosen the integration angle as the angle at which the field has decayed to -11 dB with respect to the center. This election is motivated by the fact it corresponds to a typical value of the edge taper when illuminating the subreflector of a radiotelescope.

The resulting optimal parameters are presented in Table 1. Their respective reflection losses and cross polarizations are shown in Fig. 2 and summarized in Table 2. In terms of reflection losses, the best performance is obtained with both triangular geometries. This fact comes as no surprise since the triangles allow a smoother transition from the dielectric medium to the air. The box and cylinder two-layer structures are intermediate cases, having a good performance in the entire bandwidth. Finally, the worst results are obtained for the concentric rectangular layer. It is interesting to note the low reflection losses obtained for the perpendicular triangular grooves between 67 and 80 GHz. These values suggest extremely good performance in smaller bandwidths.

The best polarization efficiencies were achieved for non-concentric designs: two-box and two-cylinder layers, and perpendicular triangular grooves. These structures introduce much less cross polarization than the concentric grooves. There are two other important facts to notice in the polarization-efficiency plot [Fig. 2(b)]. The first one is the sharp

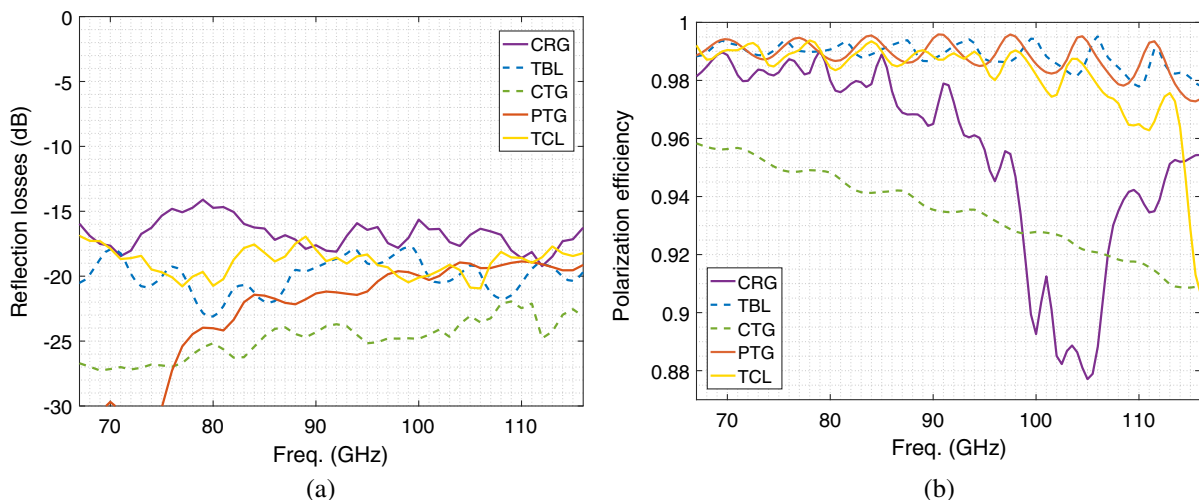


Fig. 2. Simulation results for the five antireflection layers under analysis. (a) Reflection losses. (b) Polarization efficiency integrated over a solid angle equivalent to an edge taper of -11 dB.

Table 2. Comparison of Simulated Reflexion Losses and Polarization Efficiencies for All Optimized Antireflection Layers^a

	CRG	CTG	TBL	PTG	TCL
Mean ref. loss (dB)	-16.78	-24.83	-19.98	-22.97	-18.89
Max. ref. loss (dB)	-14.10	-21.95	-17.74	-18.86	-16.95
Mean pol. eff. (%)	95.53	93.50	98.86	98.85	98.18
Min. pol. eff. (%)	87.71	90.86	97.79	97.28	90.64

^aConcentric rectangular grooves (CRG), concentric triangular grooves (CTG), two-box layer (TBL), perpendicular triangular grooves (PTG), and two-cylinder layer (TCL).

decrease of efficiency between 98 and 108 GHz for the concentric rectangular-groove layer, having a minimum at 105 GHz. This decrement is related to a standing wave between the two antireflective layers. A simple calculation reveals a direct relation between this frequency range and the thickness of the sample. We have attempted to optimize the dimensions of the rectangular grooves to eliminate this peak. It was found that to remove this cross-polarization peak a corrugation depth much smaller than $\lambda/(4n_m)$ was needed. Evidently, with such a depth the layer would lose its antireflective properties. The second fact to notice is that the cross-polarization level for the concentric triangular grooves is not optimal, but it is more constant across the full band.

3. EXPERIMENTAL VERIFICATION

Based on the simulation results we manufactured three antireflection structures over HDPE samples: concentric rectangular grooves, perpendicular triangles, and a two-cylinder layer. They are presented in Fig. 3(a). Each sample has a circular surface, with a 46-mm radius, where the antireflective layer was imprinted. The experimental strategy we followed was to directly evaluate the cross-polar contribution of the samples by introducing each one of them in the optical path of a horn-antenna characterization system. In the first experiment the beam produced by the horn antenna was fully characterized. After this calibration, the sample was introduced and the output beam was measured. Based on the two measurements we evaluated the cross polarization caused by the sample under the test. One advantage of this system is that it permits the performance

of the coating to be evaluated when facing a noncollimated beam, i.e., the usual situation in real systems.

The experimental system is presented in Fig. 3(b). The HDPE samples were mounted on a rotational stage located between an open-ended waveguide probe antenna and a horn antenna. The horn antenna is a spline corrugated device fully optimized to work on the range of 67 to 116 GHz with a cross-polar level lower than -30 dB. An orthomode transducer, described in [23], is used to select the polarization of the signal under measurement. All the involved distances in the system are larger than 5λ at the lowest frequency to avoid reactive-zone effects. The measurement system is based on a heterodyne transmitter that generates a test signal referenced to a 100-MHz base signal. The signal is received by the horn and down-converted by a receiver unit to the 100-MHz baseband. A vector network analyzer (E8364C PNA) compares the input and output intermediate frequency signal measuring the relative amplitude and phase difference. Since this is a relative measurement, no absolute calibration is required. To keep phase control of the system, a yttrium iron garnet source provides a coherent local oscillator signal to both receiver and transmitter units. The transmitter is connected to the probe antenna and attached to an XY scanner that samples a square plane perpendicular to the optical axis of the horn. A careful alignment was performed to avoid power contamination on the polarization measurements. Copolarization and cross-polarization patterns were measured by rotating the probe antenna by 90 deg. Therefore, two sets of measurements are required for each sample. The near-field data were transformed into far-field data using an algorithm based on the Fourier transform. Finally, all the data were post-processed to diminish noise by statistical analysis and calculate the polarization and antenna efficiency of the system.

Figure 4 shows the measured far-field radiation pattern at the central frequency, 95 GHz, of each configuration. Every measured far-field pattern is compared to the simulated pattern of the feed horn antenna used in the setup. Since the horn has a beam waist of 4.7 mm, we have chosen a horn-to-sample distance of 45 mm to ensure a very low truncation level. At the lowest frequency, where Gaussian beams have the highest truncations, the aperture diameter of the sample is about 6 times the beam size, which corresponds to the aperture truncating a

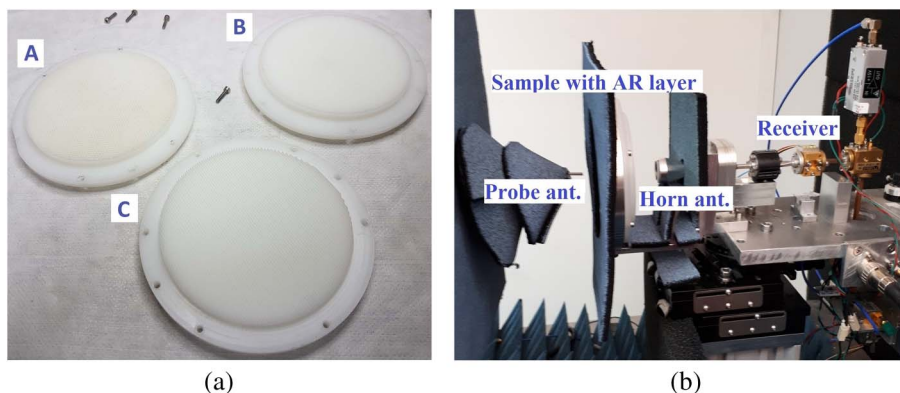


Fig. 3. (a) HDPE samples with antireflection layer: two-cylinder layers, A, concentric rectangular grooves, B, and perpendicular triangular grooves, C. (b) Near-field measurement setup.

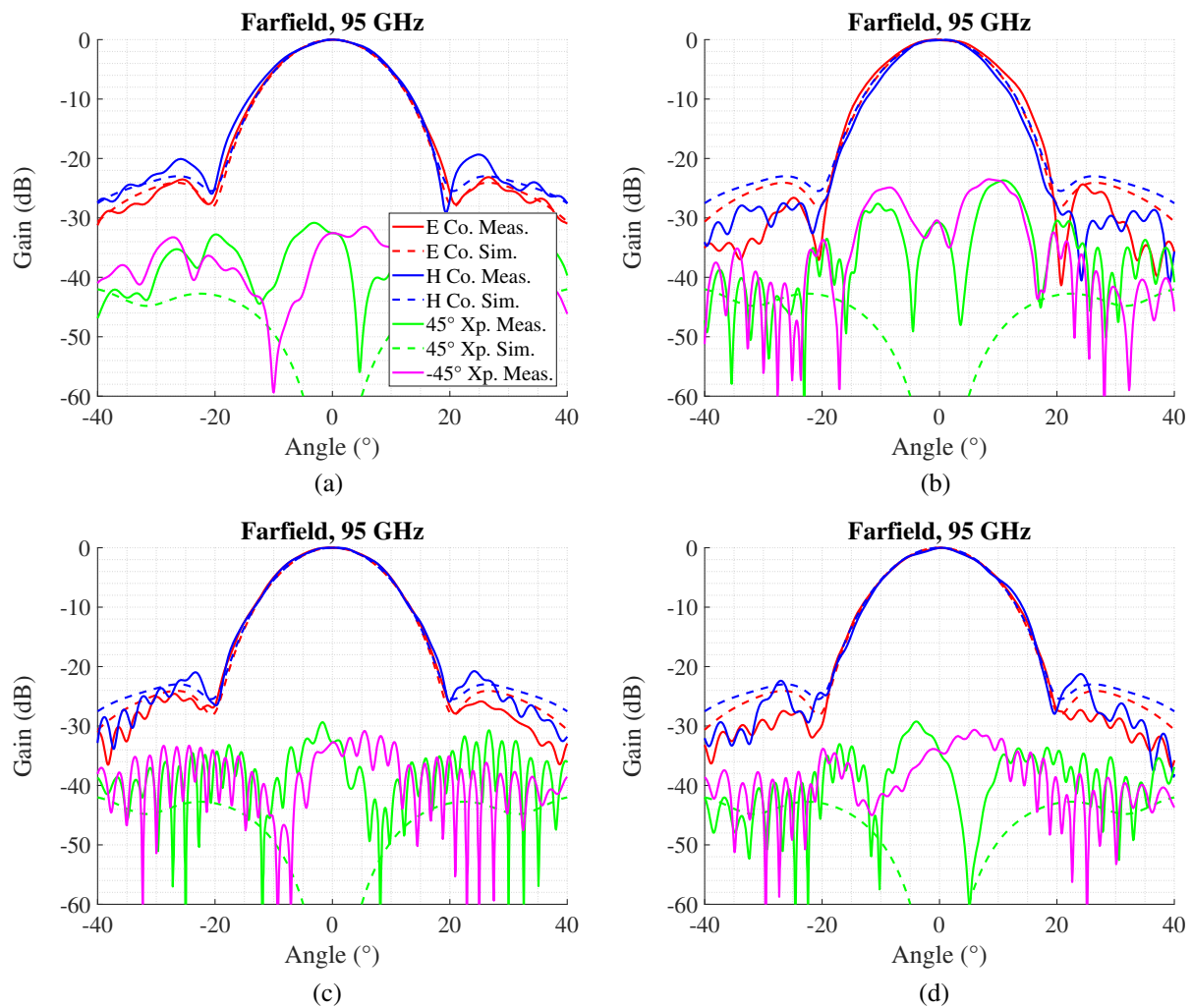


Fig. 4. Measured copolar and cross-polarization radiation patterns. (a) Only horn. (b) Horn and sample with CRG. (c) Horn and sample with PTG. (d) Horn and sample with TCL. All the measured patterns are compared to the simulation of the radiation pattern of the horn alone.

Gaussian beam at 80 dB. In the case of the horn alone [Fig. 4(a)], measured and simulated patterns show an excellent agreement. Moreover, the patterns exhibit good E- and H-plane symmetry, low sidelobes, and a cross polarization better than -31 dB. The small deviations from the simulated values can be ascribed to minimal errors in the fabrication of the horn.

The effect of including the samples, perpendicularly to the direction of propagation, is shown in panels *b* to *d* of Fig. 4. First, we can appreciate the work of the antireflective layer in the reduction of the sidelobe in the copolarization patterns, all of them having a lower level than the base case. We notice, however, important differences in their performances. On one hand, the concentric rectangular grooves increase cross polarization by about 5 dB and introduce some deformation on the main lobe of the pattern. The radiation pattern, moreover, loses symmetry between the E and H planes, and has some structures attributable to a poor matching of the layer. On the other hand, the perpendicular triangles and the two-cylinder layer do not present an important increment on the cross-polarization level. Furthermore, the good characteristics of the copolarization patterns are preserved.

For polarization analysis we have measured the copolarization and cross-polarization patterns at several frequencies from 70 to 115 GHz with a span of 5 GHz between measurement points. The experiment was repeated in a second case when the dielectric sample was tilted by 10 deg with respect to the axis of the optical system. This second measurement is used to quantify the polarization effects associated with oblique incidence to the surface. This situation is usual in optic systems where windows and filters are tilted with respect to the optical axis, avoiding unwanted reflections in the direction of the propagation. Other important cases of oblique incidence are when lenses or curved phase fronts are used. In these cases the level of cross polarization is also affected [13].

Figure 5 shows the polarization efficiency for the three fabricated antireflection layers. We can notice the degradation on the polarization efficiency for the antireflective layer made out of concentric grooves. This effect is more noticeable when the tilt is included. The other two antireflective layers introduce negligible cross polarization on the system, even when the tilt is introduced. The results have the same behavior as the

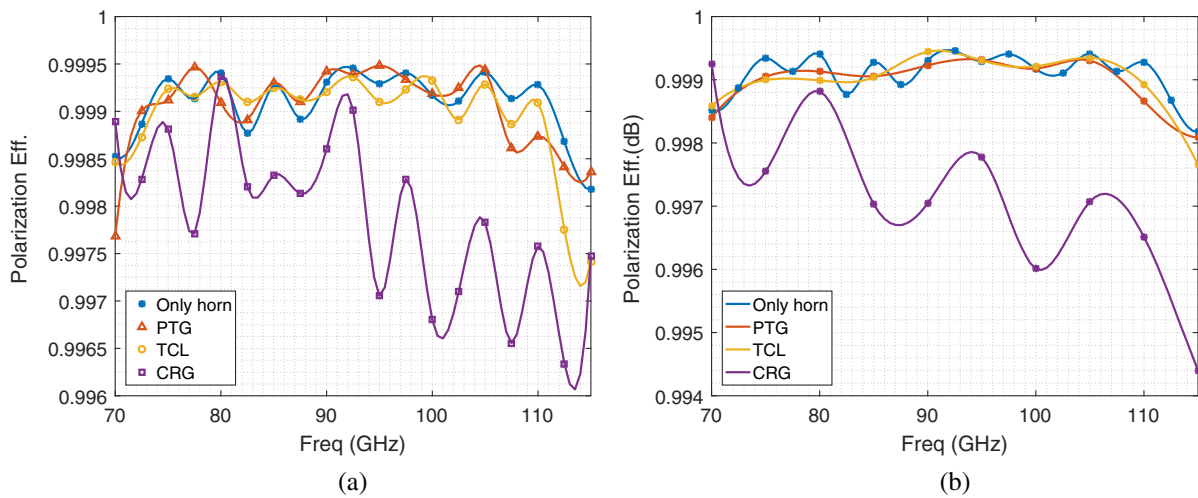


Fig. 5. Polarization efficiencies integrated over a ~ -11 dB edge taper solid angle. The measured data are interpolated using spline functions. (a) Samples perpendicular to the propagation wave. (b) Samples tilted 10 deg from the perpendicular to the propagation wave.

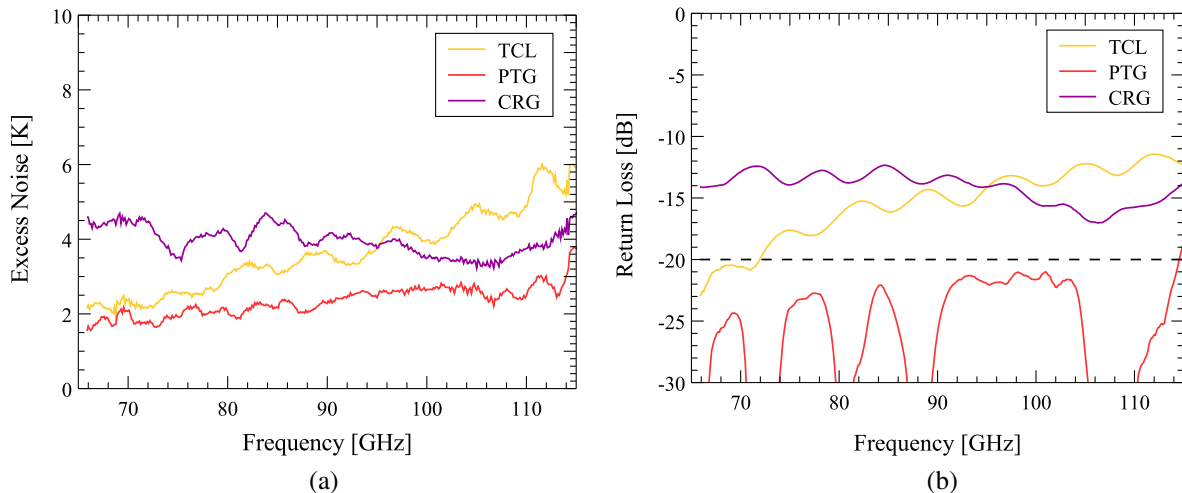


Fig. 6. (a) Measured receiver excess noise. The data has been smoothed using a bandwidth of 1.95 GHz (b) Derived return losses. The error in estimating the return losses is about 1% corresponding to -20 dB. This level is marked by the dashed line.

simulation, Fig. 2(b), but the levels are different. This is expected from the different ways the samples are illuminated, with an ideal plane wave in the simulation and a Gaussian beam from a horn antenna in the experiment.

The reflection losses of the samples were measured using a radiometric test. In this experimental system the noise temperature of a cryogenic receiver, operating at 15 K, was measured using the hot/cold method. The receiver noise temperature is around 40 K. The measurement was repeated with the antireflective sample positioned in front of the receiver's optical input. Measured results are presented in Fig. 6(a). The excess noise is due to the ohmic losses in the sample and the reflection losses of the surfaces. Ohmic losses can be easily estimated as the material properties of HDPE and sample thickness are well known. In our case we carefully measured the material properties using the filled waveguide method ($n = 2.34$

and $\tan \delta = 2.0E - 4$). Return losses were estimated using the Friis formula for system noise,

$$T_{\text{noise}} = T_{\text{phys}}(1 - L_{\text{ohmic}}) + \frac{T_{\text{RX}}}{L_{\text{ohmic}} + L_{\text{reflect}}}, \quad (2)$$

where T_{noise} is the measured noise temperature of the system including the HDPE sample, T_{phys} is the sample physical temperature, T_{rx} is the receiver noise temperature, L_{ohmic} is the ohmic loss of the material, and L_{reflect} is the return loss associated with the AR structure. In this analysis we do not consider the excess noise caused by the reflected wave termination, as it is terminated at 15 K inside the cryostat. The estimated return losses of the samples under study are presented in Fig. 6(b). These results agree with simulations, which predict the best performance for the triangular perpendicular grooves structure. [Fig. 2(a)].

4. CONCLUSIONS

We have studied five different types of antireflective layers to compare their performance in terms of return losses and cross-polarization degradation. The simulations show that the best performance is achieved with nonconcentric structures. Although concentric structures are easier to implement mechanically (e.g., with a lathe), they strongly degrade the polarization efficiency, having an important dependence on frequency.

The experimental results have confirmed the simulation results: the nonconcentric geometries characterized in this work have superior performance. They have good reflection losses and the best polarization efficiency when the appropriate geometries are chosen. Moreover, nonconcentric grooves have less frequency dependence when a tilt is applied. This could especially be critical for curved lenses where the incidence of the wave is not perpendicular to the antireflective layer, incrementing cross polarization.

In comparing the two nonconcentric structures, we have found that the perpendicular grooves perform better, especially in terms of return loss. This characteristic makes them suited for highly demanding applications such as astronomical instrumentation. However, in less demanding applications, differences are small, and selecting any of them may be based more on the simplicity of construction rather than the achieved optical performance.

Funding. Comisión Nacional de Investigación Científica y Tecnológica (CONICYT) (project Basal AFB-170002, FONDECYT 1151022, Fondo Quimal 160012); European Southern Observatory (ESO) (ESO-Chile Joint Committee).

Acknowledgment. We would like to thank J. Pizarro for his technical support and National Instrument for the donation of software licenses.

Disclosures. The authors declare that there are no conflicts of interest related to this article.

REFERENCES

1. T. Morita and S. B. Cohn, "Microwave lens matching by simulated quarter-wave transformers," *IRE Trans. Antennas Propag.* **4**, 33–39 (1956).
2. T. Takekoshi, T. Minamidani, S. Nakatsubo, T. Oshima, M. Kawamura, H. Matsuo, T. Sato, N. W. Halverson, A. T. Lee, W. L. Holzapfel, Y. Tamura, A. Hirota, K. Suzuki, T. Izumi, K. Sorai, K. Kohno, and R. Kawabe, "Optics design and optimizations of the multi-color TES bolometer camera for the ASTE telescope," *IEEE Trans. Terahertz Sci. Technol.* **2**, 584–592 (2012).
3. J. W. Lamb, "Low-noise, high-efficiency optics design for ALMA receivers," *IRE Trans. Antennas Propag.* **51**, 2035–2047 (2003).
4. A. L. Pazmany and M. Wolde, "A compact airborne G-band (183 GHz) water vapor radiometer and retrievals of liquid cloud parameters from coincident radiometer and millimeter wave radar measurements," in *Microwave Radiometry and Remote Sensing of the Environment* (2008), pp. 1–4.
5. N. Sönmez, F. Tokan, and N. T. Tokan, "Double lens antennas in millimeter-wave automotive radar sensors," *Appl. Comput. Electromagn. Soc. J.* **32**, 901–907 (2017).
6. J. Volakis, *Antenna Engineering Handbook*, 4th ed. (McGraw-Hill Education, 2007).
7. A. Schröder, A. Murk, P. Yagoubov, and F. Patt, "Design and characterization of the ALMA band 5 vacuum window," *IEEE Transactions on Terahertz Science and Technology* **6**, 156–162 (2016).
8. T. Nitta, Y. Sekimoto, K. Noda, S. Sekiguchi, S. Shu, H. Matsuo, A. Dominjon, M. Naruse, N. Kuno, and N. Nakai, "Broadband pillar-type antireflective subwavelength structures for silicon and alumina," *IEEE Trans. Terahertz Sci. Technol.* **7**, 295–301 (2017).
9. P. A. Gallardo, B. J. Koopman, N. F. Cothard, S. M. M. Bruno, G. Cortes-Medellin, G. Marchetti, K. H. Miller, B. Mockler, M. D. Niemack, G. Stacey, and E. J. Wollack, "Deep reactive ion etched anti-reflection coatings for sub-millimeter silicon optics," *Appl. Opt.* **56**, 2796–2803 (2017).
10. M. S. Mirotznik, B. L. Good, P. Ransom, D. Wikner, and J. N. Mait, "Broadband antireflective properties of inverse motheye surfaces," *IEEE Trans. Antennas Propag.* **58**, 2969–2980 (2010).
11. J. W. Lamb, "Cross-polarisation and astigmatism in matching grooves," *Int. J. Infrared Millim. Waves* **17**, 2159–2165 (1996).
12. A. González, V. Tapia, R. Finger, C. D. Huang, S. Asayama, and Y.-D. Huang, "ALMA band 1 optics (35–50 GHz): tolerance analysis, effect of cryostat infrared filters and cold beam measurements," *J. Infrared Millim. Terahertz Waves* **38**, 1215–1231 (2017).
13. P. Goldsmith, *Quasioptical Systems: Gaussian Beam Quasioptical Propagation and Applications*, IEEE Press Series on RF and Microwave Technology (Wiley, 1998).
14. D. H. Raguin and G. M. Morris, "Analysis of antireflection-structured surfaces with continuous one-dimensional surface profiles," *Appl. Opt.* **32**, 2582–2598 (1993).
15. R. Bräuer and O. Bryngdahl, "Design of antireflection gratings with approximate and rigorous methods," *Appl. Opt.* **33**, 7875–7882 (1994).
16. J. Thornton and K. Huang, *Modern Lens Antennas for Communications Engineering*, IEEE Press Series on Electromagnetic Wave Theory (Wiley, 2013), Sections 2.3.
17. V. Tapia, R. Nesti, A. González, I. Barrueto, F. P. Mena, N. Reyes, F. Villa, F. Cuttaia, and P. Yagoubov, "An ultra-broadband optical system for ALMA band 2+3," *Proc. SPIE* **9914**, 99142X (2016).
18. P. Yagoubov, A. González, V. Tapia, N. Reyes, F. P. Mena, R. Nesti, F. Cuttaia, S. Ricciardi, and F. Villa, "67–116 GHz optics development for ALMA band 2-3 receivers," in *41st International Conference on Infrared, Millimeter, and Terahertz waves (IRMMW-THz)* (2016), pp. 1–2.
19. J. W. Lamb, "Miscellaneous data on materials for millimetre and sub-millimetre optics," *Int. J. Infrared Millim. Waves* **17**, 1997–2034 (1996).
20. R. Datta, C. D. Munson, M. D. Niemack, J. J. McMahon, J. Britton, E. J. Wollack, J. Beall, M. J. Devlin, J. Fowler, P. Gallardo, J. Hubmayr, K. Irwin, L. Newburgh, J. P. Nibarger, L. Page, M. A. Quijada, B. L. Schmitt, S. T. Staggs, R. Thornton, and L. Zhang, "Large-aperture wide-bandwidth antireflection-coated silicon lenses for millimeter wavelengths," *Appl. Opt.* **52**, 8747–8758 (2013).
21. V. Tapia, A. González, R. Finger, F. P. Mena, D. Monasterio, N. Reyes, M. Sánchez, and L. Bronfman, "High efficiency wideband refractive optics for ALMA band-1 (35–52 GHz)," *J. Infrared Millim. Terahertz Waves* **38**, 261–275 (2017).
22. O. Kilic, M. S. Mirotznik, and B. Good, "Bio-inspired optimization techniques for the design of millimeter wave antireflective surfaces," in *Proceedings of the Fourth European Conference on Antennas and Propagation (EuCAP)* (2010), pp. 1–3.
23. F. M. I. Barrueto, N. Reyes, and L. Bronfman, "A broadband ortho-mode transducer for the new ALMA band 2+3 (67–116 GHz)," in *9th Global Symposium on Millimeter Waves (GSMW) & 7th ESA Workshop on Millimetre-Wave Technology and Applications* (2016), pp. 1–4.